From dark matter halos to pre-stellar cores: high resolution follow-up of cosmological Lyman–Werner simulations

Lewis R. Prole,[1]* Anna T. P. Schauer [ID],[2]* Paul C. Clark [ID],[1] Simon C. O. Glover [ID],[3]* Felix D. Priestley[1] and Ralf S. Klessen [ID][3,4]

[1]*Cardiff School of Physics and Astronomy, Cardiff University, Trevithick Building, The Parade, Cardiff CF24 3AA, UK*
[2]*Department of Astronomy, The University of Texas at Austin, Austin, TX 78712, USA*
[3]*Universität Heidelberg, Zentrum für Astronomie, Institut für Theoretische Astrophysik, Albert-Ueberle-Straße 2, D-69120 Heidelberg, Germany*
[4]*Universität Heidelberg, Interdisziplinäres Zentrum für Wissenschaftliches Rechnen, Im Neuenheimer Feld 205, D-69120 Heidelberg, Germany*

ABSTRACT

Molecular hydrogen allows cooling in primordial gas, facilitating its collapse into Population III stars within primordial halos. Lyman–Werner (LW) radiation from these stars can escape the halo and delay further star formation by destroying H_2 in other halos. As cosmological simulations show that increasing the background LW field strength increases the average halo mass required for star formation, we perform follow-up simulations of selected halos to investigate the knock-on effects this has on the Population III IMF. We follow 5 halos for each of the $J_{21} = 0$, 0.01, and 0.1 LW field strengths, resolving the pre-stellar core density of 10^{-6} g cm^{-3} (10^{18} cm^{-3}) before inserting sink particles and following the fragmentation behaviour for hundreds of years further. We find that the mass accreted onto sinks by the end of the simulations is proportional to the mass within the $\sim 10^{-2}$ pc molecular core, which is not correlated to the initial mass of the halo. As such, the IMFs for masses above the brown dwarf limit show little dependence on the LW strength, although they do show variance in the number of low-mass clumps formed. As the range of background LW field strengths tested here covers the most likely values from literature, we conclude that the IMF for so-called Pop III.2 stars is not significantly different from the initial population of Pop III.1 stars. The primordial IMF therefore likely remains unchanged until the formation of the next generation of Population II stars.

Key words: hydrodynamics – software: simulations – stars: luminosity function, mass function – software: simulations – dark ages, reionization, first stars.

1 INTRODUCTION

This first stars are able to form because pristine baryonic gas can collapse within the gravitational potential well of dark matter (DM) halos (Couchman & Rees 1986; Haiman, Thoul & Loeb 1996a; Tegmark et al. 1997), heating it to ~ 5000 K and facilitating the formation of H_2 (Bromm, Coppi & Larson 2002). H_2 primarily forms via the radiative association reaction forming H^-

$$H + e^- \rightarrow H^- + \gamma, \tag{1}$$
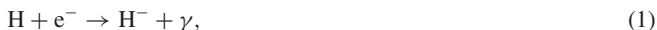
followed by the fast associative detachment reaction forming H_2

$$H^- + H \rightarrow H_2 + e^-. \tag{2}$$

Radiative cooling from the molecular hydrogen renders the gas gravitationally unstable, which allows it to decouple from the DM and collapse to form the first stars, known as Population III (Pop III) stars. The necessity of H_2 renders any process of H_2 destruction as a mechanism to delay or prevent Pop III star formation.

While so-called Pop III.1 stars form from purely cosmological initial conditions, the radiation they produce affects Pop III.2 stars

that form in its presence. As the masses of Pop III stars are predicted to be larger than present-day counterparts (due to the lack of cooling from dust and metals), they are expected to emit large amounts of ionizing radiation (e.g. Schaerer 2002). Ionizing photons above the Lyman limit (13.6 eV) create H II regions around the stars up to the boundary of their Strömgren spheres (Whalen, Abel & Norman 2004; Kitayama et al. 2004; Alvarez, Bromm & Shapiro 2006; Abel, Wise & Bryan 2007; Yoshida et al. 2007a; Jaura et al. 2022) while photons below the Lyman limit are free to escape their Strömgren sphere. Lyman–Werner (LW) photons between 11.2 and 13.6 eV can dissociate H_2 via the two-step Solomon process (Field, Somerville & Dressler 1966; Stecher & Williams 1967)

$$H_2 + \gamma \rightarrow H_2^* \rightarrow 2H, \tag{3}$$

where H_2^* represents an electronically excited state of H_2. Photons with energy above 0.76 eV can also photodissociate H^- via

$$H^- + \gamma \rightarrow H + e^-, \tag{4}$$

reducing the H^- abundance and hence the rate at which H_2 can form via reaction (2) (e.g. Chuzhoy, Kuhlen & Shapiro 2007). This stellar feedback provides a potential obstacle for Pop III.2 stars to overcome during formation. Investigations into the effects of these far UV fields

* E-mail: prolel@cardiff.ac.uk (LRP); anna.schauer@utexas.edu (ATPS); glover@uni-heidelberg.de (SCOG)

typically categorize the field strength by the intensity in the LW band J_{21}, in units of 10^{-21} erg s^{-1} cm^{-2} Hz^{-1} sr^{-1}.

Calculations by Haiman, Rees & Loeb (1997) found that before the Strömgren spheres of Pop III stars overlap, the UV background below the ionization threshold was able to penetrate large clouds and suppress their H$_2$ abundance. They also found that the flux necessary for H$_2$ photodissociation is several orders of magnitude smaller than the flux needed to reionize the universe. Haiman, Abel & Rees (2000) showed that this photodissociation of H$_2$ suppresses further Pop III star formation inside small halos and delays reionization until larger halos form.

Collapse is not impossible without sufficient H$_2$ for cooling. Omukai (2001) showed that if the LW field is sufficient to keep a halo free of molecular hydrogen, the gas can nevertheless collapse via atomic hydrogen line cooling if the halo has a virial temperature $T_{vir} > 8000$ K. The collapse occurs almost isothermally, possibly resulting in the formation of a direct collapse black hole (DCBH) (e.g. Bromm & Loeb 2003; Spaans & Silk 2006; Latif et al. 2013), a possible progenitor of the supermassive black holes observed at high redshifts (e.g. Mortlock et al. 2011; Matsuoka et al. 2019). However, for a T $= 10^5$ K blackbody spectrum expected from Pop III stars, a field strength of $J_{21} \sim 10^4$ is required to keep the gas atomic during the collapse (Glover 2015; Agarwal & Khochfar 2015; Agarwal et al. 2016; Sugimura, Omukai & Inoue 2014), while the average exposure is expected to be $J_{21} < 0.1$ at $z \sim 15$ (Ahn et al. 2009; Trenti & Stiavelli 2009; Wise et al. 2012; Agarwal et al. 2012; Skinner & Wise 2020). Dijkstra et al. (2008) showed that only a fraction of $10^{-8} - 10^{-6}$ of DM halos with virial temperatures $> 10^4$ K have a close luminous neighbour within < 10 kpc, and are exposed to an LW flux $J_{21} > 10^3$. The occurrence of atomically cooled halos is therefore expected to be rare.

Studies have shown that values of J_{21} orders of magnitude lower than the critical intensity required to completely suppress H$_2$ cooling in massive halos can still drastically affect halo collapse. Typically, the critical mass for efficient molecular hydrogen cooling and subsequent star formation increases with increasing J_{21} (e.g. Machacek, Bryan & Abel 2001; Yoshida et al. 2003; O'Shea & Norman 2008; Visbal et al. 2014; Schauer et al. 2021). Cosmological simulations by Yoshida et al. (2003) found gas cooling was suppressed for $J_{21} = 0.1$, leading them to predict that star formation would not occur in halos with $T_{vir} < 8000$ K for LW field strengths greater than this. Conversely, O'Shea & Norman (2008) found that for field strengths as high as $J_{21} = 1$, H$_2$ cooling leads to collapse despite the depressed core molecular hydrogen fractions. They also noted that higher LW background fluxes lead to higher accretion rates. High-resolution cosmological simulations by Schauer et al. (2021) (hereafter AS21) examined the impact of different values of the LW field strength on a large sample of minihalos. They showed that both M$_{av}$, the average minihalo mass required for efficient H$_2$ cooling (i.e. the mass above which more than 50 per cent of minihalos of that mass can cool), and M$_{min}$, the minimum minihalo mass required for efficient cooling, increased with increasing J_{21}. An increase in the critical halo mass for star formation with increasing J_{21} was also found by Kulkarni, Visbal & Bryan (2021), although they find a significant effect only for $J_{21} > 1$. In contrast, cosmological simulations by Skinner & Wise (2020) found no relationship between the LW intensity and host halo mass.

The true average J_{21} intensity is expected to vary with redshift. Hirano et al. (2015) followed the formation and evolution of 1540 star-forming gas clouds. They found that in their models, the characteristic mass of Pop III stars shifted to lower masses with decreasing redshift due to the radiative feedback of previous generations of stars. For $z > 20$, half of the star-forming gas clouds were exposed to intense FUV radiation, with an average exposure of $J_{21} \sim 0.07$. Due to smaller stellar masses and the expanding distance between stars, the FUV background became weaker at lower redshifts. For $15 < z < 25$, almost all the clouds had non-zero intensity $J_{21} > 0.01$. The average LW intensity in Skinner & Wise (2020) increased stochastically from 10^{-3} at $z \sim 25$ to 10 at $z \sim 10$. For redshifts above ~ 12, J_{21} remained > 0.1.

Self-shielding is a process that occurs when large column density of molecular hydrogen protects the inner regions against photodissociation because one photon can only photodissociate one H$_2$ molecule. This self-shielding allows further H$_2$ production and H$_2$ cooling (Shang, Bryan & Haiman 2010; Agarwal et al. 2014; Regan, Johansson & Wise 2014; Hartwig et al. 2015a). The large non-equilibrium abundance of electrons in gas cooling from above T $> 10^4$ K also boosts H$_2$ formation (Oh & Haiman 2002). Early attempts to model self-shielding (e.g. Shang et al. 2010) multiplied the intensity in the LW band by a self-shielding factor given by Draine & Bertoldi (1996). Wolcott-Green, Haiman & Bryan (2011) showed that this method underestimated the numerically calculated self-shielding rate by more than an order of magnitude in low-density regions, by overestimating shielding by a large factor at temperatures above a few hundred kelvin. They modified the method of Draine & Bertoldi by estimating the shielding factor based on the Sobolev length, using local properties of the gas. This modification was computationally inexpensive and used in many subsequent investigations into the aforementioned critical intensity required to form atomic halos, typically producing values an order of magnitude lower than those using the original Draine & Bertoldi shielding (e.g. Glover 2015; Agarwal & Khochfar 2015; Agarwal et al. 2016). Clark, Glover & Klessen (2012) improved on this method further with their introduction of the TreeCol algorithm, which calculates maps of the column density distribution seen by each computational element in a simulation in a computationally efficient fashion with the help of an oct-tree. Hartwig et al. (2015b) took this approach further by accounting for the relative velocities between different computational elements. This Doppler-shifts the spectral lines, reducing the effectiveness of self-shielding (since molecules shifted by more than the linewidth do not contribute to the effective column density).

In addition to a background LW field, primordial star formation is complicated further by streaming velocities between the the gas and DM. Prior to recombination, baryons were tightly coupled to photons. As DM does not experience Thomson scattering, there should have been a relative velocity between the DM and baryons (e.g. Ma & Bertschinger 1995). At recombination, the relative velocity was ~ 30 km s^{-1} and was coherent over several comoving Mpc. Recombination resulted in a drop in the sound speed to ~ 6 km s^{-1} as the gas transitioned from plasma to a neutral state, meaning the relative velocities were highly supersonic. Tseliakhovich & Hirata (2010) showed that the presence of these large-scale streaming velocities suppresses the abundance of the first bound objects by advecting small-scale perturbations near the baryonic Jeans scale. Moving-mesh calculations by Greif et al. (2011) found that the additional momentum and energy from the streaming velocities reduces the gas fractions and central densities of halos, increasing the typical virial mass required for efficient cooling by a factor of three. They also noted that the turbulent velocity dispersion increased in the presence of streaming velocities. The simulations of AS21 found that the increase in the average and minimum halo mass from increasing streaming velocities is additive on top of the effect of a LW field, with streaming velocities having the larger impact of the two.

While it was initally believed that Pop III stars formed in isolation (Haiman, Thoul & Loeb 1996b) and were massive (Abel, Bryan & Norman 2002; Bromm et al. 2002), more recent studies show that primordial gas fragments to give rise to a larger populations of lower mass stars (Clark et al. 2011; Smith et al. 2011; Greif et al. 2012; Stacy & Bromm 2013; Machida & Doi 2013; Stacy et al. 2014; Susa 2019; Wollenberg et al. 2020). In Prole et al. (2022a) (hereafter LP22), we used high-resolution simulations of idealized, purely hydrodynamical Pop III star formation to show that a number of cores are ejected from the system with masses capable of surviving until the present day. As small-scale primordial magnetic fields do not appear to prevent disc fragmentation (Prole et al. 2022b) and accretion of metals onto the surface of these stars during their lifetime is unlikely (e.g. Johnson & Khochfar 2011; Tanaka et al. 2017), the question is raised about why these stars have not been found within archeological surveys (see e.g. Beers & Christlieb 2005; Frebel & Norris 2015; Starkenburg et al. 2017). Since most high-resolution simulations of Pop III star formation have considered only the Pop III.1 case, one possible explanation could be that Pop III.2 star formation yields a different IMF, that is, that Pop III stars forming in the presence of a LW background have systematically larger masses than those forming in the absence of a background.

In this paper, we aim to test this hypothesis by producing the most accurate prediction of the Pop III.1 and Pop III.2 initial mass functions (IMFs) to date. We investigate how the increase in halo masses due to increasing LW field intensity changes star formation within them, by performing high resolution follow-up simulations of cosmological halos drawn from the simulations of AS21. The structure of our paper is as follows. In Section 2, we describe the cosmological simulations of AS21, our selection criteria for the halos chosen for follow-up simulations, the chemical model we use and our use of sink particles. In Section 3, we review the characteristics of the halos as they are taken from AS21, before presenting the results of the zoom-in simulations in Section 4, where we probe the density regime of the molecular core. In Section 5, we compare the fragmentation behaviour once sink particles have formed and present the IMFs at the end of the simulations. We discuss caveats in Section 6 before concluding in Section 7.

2 NUMERICAL METHOD

2.1 AREPO

The simulations presented here were performed with the moving mesh code AREPO (Springel 2010) with a primordial chemistry set-up. AREPO combines the advantages of AMR and smoothed particle hydrodynamics (SPH: Monaghan 1992) with a mesh made up of a moving, unstructured, Voronoi tessellation of discrete points. AREPO solves hyperbolic conservation laws of ideal hydrodynamics with a finite volume approach, based on a second-order unsplit Godunov scheme with an exact Riemann solver. Automatic and continuous refinement overcome the challenge of structure growth associated with AMR (e.g. Heitmann et al. 2008).

2.2 Cosmological simulations

The cosmological simulations performed by AS21 assumed a ΛCDM cosmology with parameters $h = 0.6774$, $\Omega_0 = 0.3089$, $\Omega_b = 0.04864$, $\Omega_\Lambda = 0.6911$, $n = 0.96$, and $\sigma_8 = 0.8159$ as derived by the Planck Collaboration et al. (2020). The simulations were initialized at $z = 200$ with an initial DM distribution created by MUSIC (Hahn & Abel 2011) using the transfer functions of Eisenstein & Hu (1998)

and the gas distribution initially followed the DM. The DM was represented by 1024^3 particles and the gas was initially modelled with 1024^3 grid cells, all contained within a box with side length $1\,h^{-1}$ Mpc in comoving units. During the simulation, an additional Jeans refinement criterion was applied: cells were refined whenever necessary so as to ensure that the Jeans length was always resolved with at least 16 cells. This refinement was carried out until the gas reached a threshold density of $\sim 10^{-19}$ g cm^{-3}. Above this threshold density, gravitationally bound and collapsing gas was converted into collisionless sink particles, as explained at greater length in AS21. The simulations were carried out with four different values of the baryonic streaming velocity ($v_{str} = 0$, 1, 2, and 3, in units of σ_{rms}, the large-scale rms value) and three different values for the LW field strength ($J_{21} = 0$, 0.01, and 0.1). In this study, we make use of the three simulations with $v_{str} = 1\sigma_{rms}$ because this is the most representative value available, as the volume fraction of streaming velocities peaks at $0.8\sigma_{rms}$ (AS21).

2.3 Halo selection

Given snapshots at $z = 15$ from the three simulations with $v_{str} = 1$ presented in AS21, we have selected five halos for each value of J_{21}. Halo positions and masses were provided by the friends-of-friends (FoF) algorithm as described in that study. The selection criteria for the halos was as follows:

(i) The halos identified by the FoF algorithm were sorted by their mass difference with M_{av}, the average minihalo mass above which minihalos become capable of cooling and forming stars. This average mass was defined in AS21, following Schauer et al. (2019), to be the minihalo mass above which more than 50 per cent of minihalos can cool and form stars.[1] AS21 report M_{av} at a range of redshifts between $z = 22$ and $z = 14$; here, we adopt their values at $z = 15$. By sorting the halos in this way, we ensure that the halos that we eventually select will have masses close to M_{av}, that is, that they are representative of the common case at that redshift.

(ii) We considered a halo if it contained a cell denser than $\rho_{th} = 10^{-22}$ g cm^{-3} within a search radius $R_{search} = 1$ kpc in physical units from the halo's central coordinate. Note that checking the H_2 abundance is not necessary, as collapse to this density is not possible without a high-H_2 abundance outside of the atomically cooling halo scenario.

(iii) We check that the halo is sufficiently resolved, that is, the 16 cells per Jeans length criteria has not decreased as the cell sizes approach the maximum resolution of the cosmological simulations. This process begins when the density reaches $\sim 10^{-20}$ g cm^{-3}, so we reject halos including a cell above this density. Note that this also ensures that a sink particle has not yet been formed within R_{search}.

(iv) Lastly, we removed the halo from consideration if there were other dense objects in the vicinity by checking there were no cells above ρ_{th} within the radius $R_{search}/2 < r < R_{search}$.

We performed this search throughout the simulation cube until five suitable halos were selected for each J_{21} value. After converting the units from comoving to physical, we cropped a 2 kpc box around each of the halos for our zoom-in simulations. The selected halo masses from each simulation are shown in Table 1. Mass-weighted mean temperatures and H_2 abundances are plotted as a function of density for each halo in Fig. 1 and radial distributions of enclosed gas and

---

[1]Note that M_{av} is typically around a factor of three larger than M_{min}, the mass of the least massive minihalo with cool gas.

Table 1. Total mass (DM and gas) as detected by the FoF algorithm within the selected halos from AS21.

	$J_{21} = 0$	$J_{21} = 0.01$	$J_{21} = 0.1$
Halo		M_{tot} [$10^6\,M_\odot$]	
1	3.50	4.76	8.70
2	3.65	4.84	8.30
3	2.81	4.30	6.70
4	2.76	4.02	4.15
5	2.96	3.91	3.90

DM along with velocity information are shown in Fig. 2. Projections of the initial density, temperature, and H_2 abundance distributions are visualized in Figs 3, 4, and 5. Note that all of these figures show the state of the halos at the point at which we extract them from the AS21 simulations, that is, prior to our zoom-in calculation. Our choice of selection criteria means that the same halos are not chosen for direct comparison between each simulation. Rather, they are chosen to be most representative of the universe at the given background LW field strength. Direct comparison also has the drawback that individual halos will collapse at different redshifts depending on the LW field strength, whereas we exclusively select halos that become able to form stars at $z = 15$.

2.4 Chemistry

Collapse of primordial gas is closely linked to the chemistry involved (e.g. Glover, Savin & Jappsen 2006; Yoshida, Omukai & Hernquist 2007b; Glover & Abel 2008; Turk et al. 2011). We therefore use a fully time-dependent chemical network to model the gas. We use the same chemistry and cooling as Wollenberg et al. (2020), which is described in the appendix of Clark et al. (2011), but with updated rate coefficients, as summarized in Schauer et al. (2019). The network has 45 chemical reactions to model primordial gas made up of 12 species: H, H^+, H^-, H_2^+, H_2, He, He^+, He^{++}, D, D^+, HD, and free electrons. Optically thin H_2 cooling is modelled as described in Glover & Abel (2008): we first calculate the rates in the low density ($n \rightarrow 0$) and LTE limits, and the smoothly interpolate between them as a function of n/n_{cr}, where n_{cr} is the H_2 critical density. To compute the H_2 cooling rate in the low-density limit, we account for the collisions with H, H_2, He, H^+, and electrons. To calculate the H_2 cooling rate in the optically thick limit, we use an approach introduced by Yoshida et al. (2006), as described in detail in Clark et al. (2011). Prior to the simulation, we compute a grid of optically thick H_2 cooling rates as a function of the gas temperature and H_2 column density. During the simulation, if the gas is dense enough for the H_2 cooling to potentially be in the optically thick regime ($\rho > 2 \times 10^{-16}\,\mathrm{g\,cm^{-3}}$), we interpolate the H_2 cooling rate from this table, using the local gas temperature and an estimate of the effective H_2 column density computed using the Sobolev approximation. In addition to H_2 cooling, we also account for several other heating and cooling processes: collisionally-induced H_2 emission, HD cooling, ionization and recombination, heating and cooling from changes in the chemical make-up of the gas and from shocks, compression and expansion of the gas, three-body H_2 formation, and heating from accretion luminosity. For reasons of computational efficiency, the network switches off tracking of deuterium chemistry[2] at densities above $10^{-16}\,\mathrm{g\,cm^{-3}}$, instead assuming that the ratio of HD to H_2 at these densities is given by the cosmological D to H ratio of

---

[2]Note that HD cooling continues to be included in the model.

2.6×10^{-5}. The adiabatic index of the gas is computed as a function of chemical composition and temperature with the AREPO HLLD Riemann solver.

As in AS21, we use a radiation field expected from massive Pop III stars. We use a blackbody spectrum at temperature 10^5 K for energies below 13.6 eV. Above this energy, the flux is expected to drop due to absorption in the intergalactic medium, so we set the value of the radiation field to 0 above 13.6 eV. We model the effects of H_2 self-shielding using the TreeCol algorithm (Clark et al. 2012).

2.5 Sink particles

If the local Jeans length falls below the minimum cell size of the mesh, artificial collapse occurs. We insert sink particles into the simulations at a threshold density to prevent artificial collapse when the simulation reaches its maximum refinement level. Our sink particle implementation was introduced in Wollenberg et al. (2020) and Tress et al. (2020). A cell is converted into a sink particle if it satisfies three criteria: (1) it reaches a threshold density; (2) it is sufficiently far away from pre-existing sink particles so that their accretion radii do not overlap; and (3) the gas occupying the region inside the sink is gravitationally bound and collapsing. Likewise, for the sink particle to accrete mass from surrounding cells it must meet two criteria: (1) the cell lies within the accretion radius; and (2) it is gravitationally bound to the sink particle. A sink particle can accrete up to 90 per cent of a cell's mass, above which the cell is removed and the total cell mass is transferred to the sink.

Increasing the threshold density for sink particle creation drastically increases the degree of fragmentation, reducing the masses of subsequent secondary protostars (LP22). Ideally, sink particles would be introduced when the gas becomes adiabatic at $\sim 10^{-4}\,\mathrm{g\,cm^{-3}}$. This is currently computationally challenging. However, the zero metallicity protostellar model of Machida & Nakamura (2015) suggests that stellar feedback kicks in to halt collapse at $\sim 10^{-6}\,\mathrm{g\,cm^{-3}}$ ($10^{18}\,\mathrm{cm^{-3}}$), so we choose this as our sink particle creation density.

The initial accretion radius of a sink particle R_{sink} is chosen to be the Jeans length λ_J corresponding to the sink particle creation density and corresponding temperature. At $10^{-6}\,\mathrm{g\,cm^{-3}}$, we take the temperature value from LP22 of 4460 K to give a Jeans length of 1.67×10^{12} cm. We set the minimum cell length to fit eight cells across the sink particle in compliance with the Truelove condition, by setting a minimum cell volume $V_{min} = (R_{sink}/4)^3$. The minimum gravitational softening length for cells and sink particles L_{soft} is set to $R_{sink}/4$.

The increasing radius of a Pop III protostar is dependent on both its mass and accretion rate (e.g. Omukai & Palla 2003; Hosokawa & Omukai 2009; Hosokawa, Omukai & Yorke 2012; Hirano et al. 2014). We allow the sink particle accretion radius R_{sink} to vary throughout its accretion history, using on-the-fly calculations of the stellar radius using an approximate analytic formulae originally derived by Stahler, Palla & Salpeter (1986):

$$R_{sink} = 26 R_\odot \left(\frac{M}{M_\odot} \right)^{0.27} \left(\frac{\dot{M}}{10^{-3}\,M_\odot \mathrm{yr}^{-1}} \right)^{0.41}, \tag{5}$$

where we smooth $\dot{M}$ by taking the average over the time taken to accrete $0.1\,M_\odot$.

The sink particle treatment also includes the accretion luminosity feedback from Smith et al. (2011), as implemented in AREPO by Wollenberg et al. (2020). Stellar internal luminosity is not included in this work because the Kelvin–Helmholtz times of the
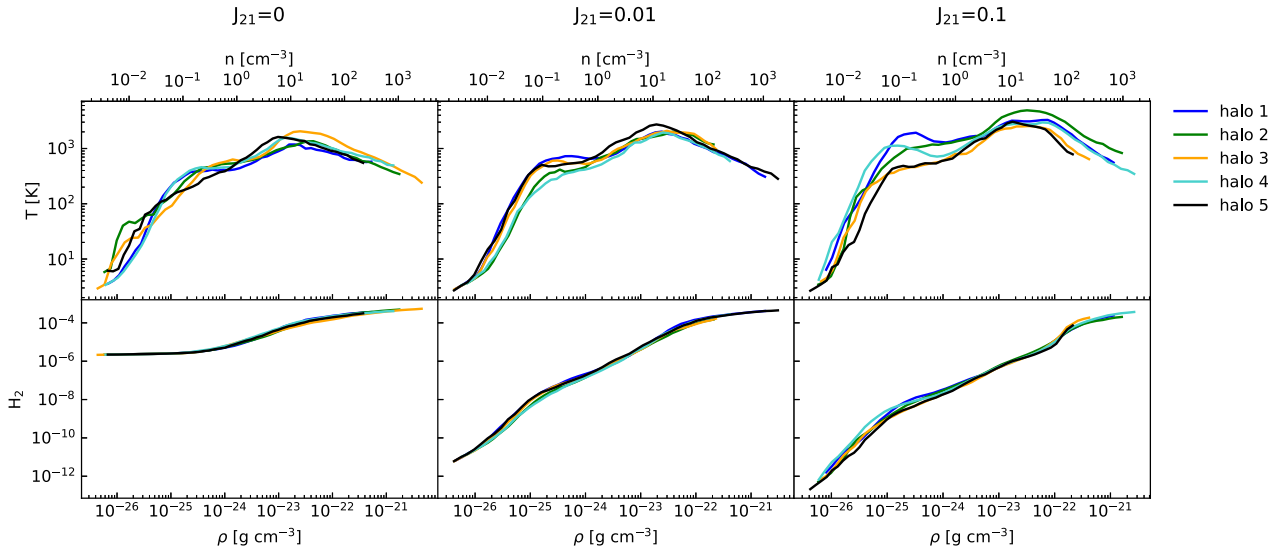
Figure 1. Summaries of the initial conditions for our simulations. Mass-weighted density profiles of temperature and H_2 abundances.
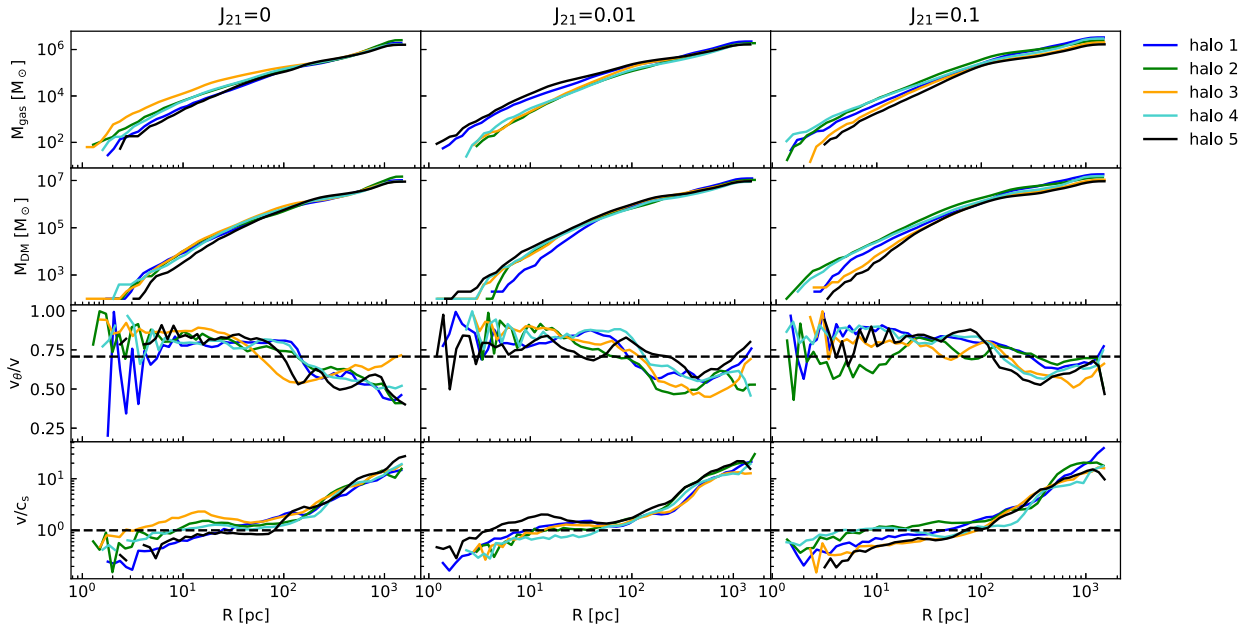

Figure 2. Summaries of the initial conditions for our simulations. Cumulative radial profiles of gas and DM mass and mass-weighted radial profiles of the ratio of rotational to total velocity (note the dotted line represents the value above which rotational component dominates the velocity) and ratio of velocity to sound speed, that is, Mach number.

protostars formed in our simulations are much longer than the period simulated, meaning that none will have yet begun nuclear burning. We also include the treatment of sink particle mergers used in LP22.

3 INITIAL HALO CHARACTERISTICS

Figs 1 and 2 show some of the characteristics of the halos at the time when they were selected for zoom-in follow-up simulations. The top panel of Fig. 1 shows that the gas has already been shock heated as it fell into the gravitational potential well of the DM halo, allowing it to produce the necessary H_2 to cool and collapse to higher densities. The bottom panel shows the destructive impact of the LW radiation field on the H_2 abundance in the outer regions

of the halo. The H_2 abundance in the central regions reaches the same peak value of 4×10^{-4} due to self-shielding from the radiation field, however, this happens at increasingly higher densities for larger J_{21} values. Fig. 2 shows that within $\sim$100 pc, the gas velocity is dominated by the component perpendicular to the radius vector, v_θ. The gas surrounding the halos is highly supersonic due to large-scale streaming, which cascades down to become subsonic at scales smaller than $\sim$10 pc, although we show in Section 4 that the velocities do not remain subsonic once the gas collapses further. From the density projections of Fig. 3, halo sizes range from $\sim$100 to 200 pc, their shapes range from roughly spherical to structurally complex, and each is embedded within a network of filamentary structures. Fig. 4 shows that these webs of filaments are a few hundred kelvin hotter than the $\sim$10 K gas that surrounds them, with the central
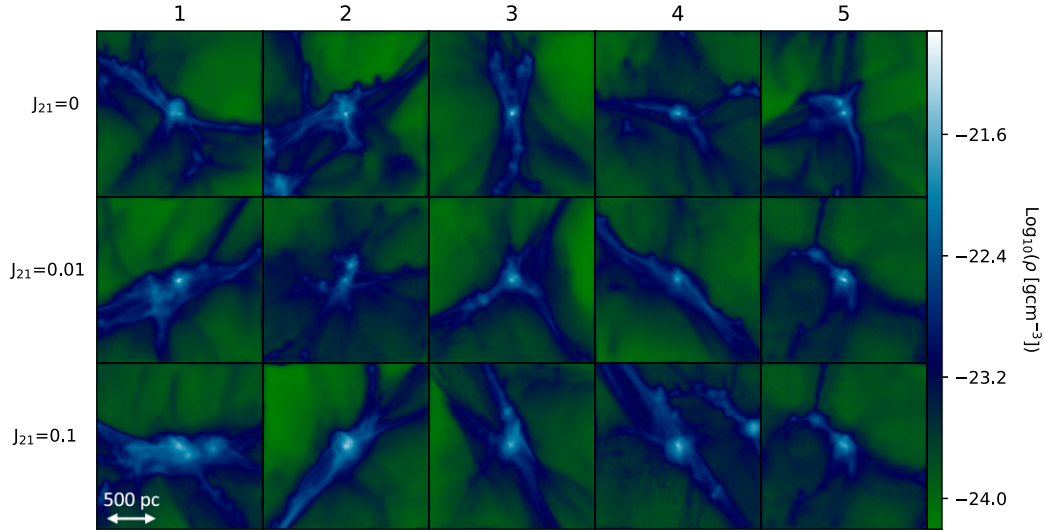
Figure 3. Column-weighted density projections of the 2 kpc region around the 5 cosmological halos for each J_{21} value, taken from AS21, which serve as the initial conditions of the high resolution follow-up simulations presented in this work. The halo numbers to compare with upcoming plots are indicated at the top of the figure.
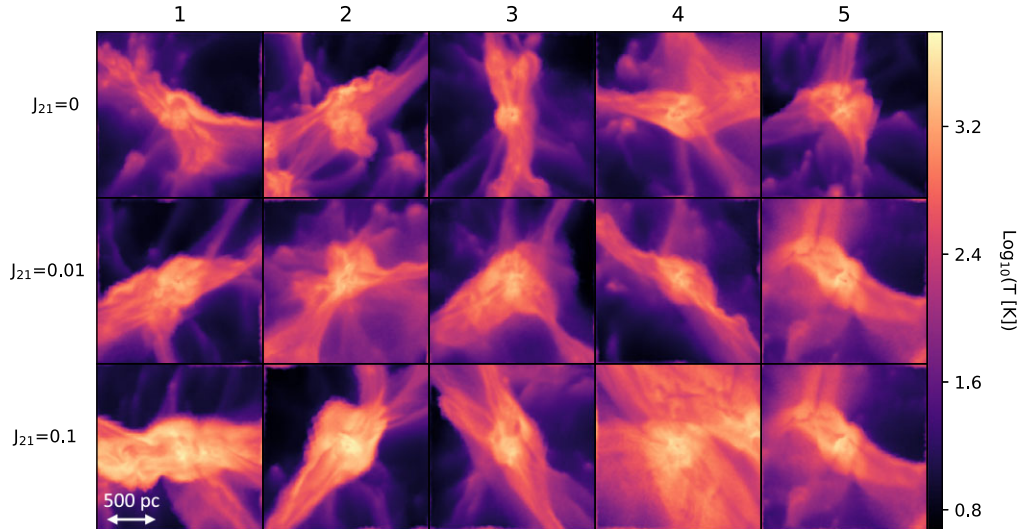

Figure 4. Column-weighted temperature projections of the 2 kpc region around the 5 cosmological halos for each J_{21} value, taken from AS21, which serve as the initial conditions of the high resolution follow-up simulations presented in this work.

halo reaching $\sim 1000 - 2000$ K. Fig. 5 shows how the background H_2 abundance is reduced drastically by the LW background, with significant levels of H_2 only appearing in the central regions of the halo.

4 FURTHER COLLAPSE

We continue the collapse down to densities of 10^{-6} g cm^{-3} before inserting sink particles. Fig. 6 shows temperature and chemical abundance profiles as a function of density, just before the formation of the first sink particle. At densities above 10^{-15} g cm^{-3}, three-body H_2 formation raises its abundance to over 0.1 within the *molecular core*. The abundance of free electrons falls off with density as the gas recombines. Fig. 7 shows radial profiles of density and velocity. The rotational component of the gas velocity remains dominated by rotation only down to scales of ~ 1 pc, below which infall begins to

dominate. The velocities remain supersonic down to scales of 10^{-6} pc (0.2 au). Halos experiencing a LW field are capable of achieving higher velocities, likely due to the higher halo mass.

The left hand side of Fig. 8 compares the temperature, density, accretion time-scale, and H_2 abundance radial profiles for the different J_{21} values just before the formation of the first sink particle. Stronger LW fields require higher mass halos for star formation, as their stronger gravitational potential is capable of shock-heating the gas to higher temperatures, which increases the H_2 formation rate enough to build up a high-column density of H_2 in order to self-shield the collapsing regions. Despite larger halo masses and shock-heating to higher initial temperatures, the density profile of the gas remains unaffected. Following Abel et al. (2002) and O'Shea & Norman (2008), we have also estimated the accretion time-scale ($t_{acc} = M/\dot{M}$), where
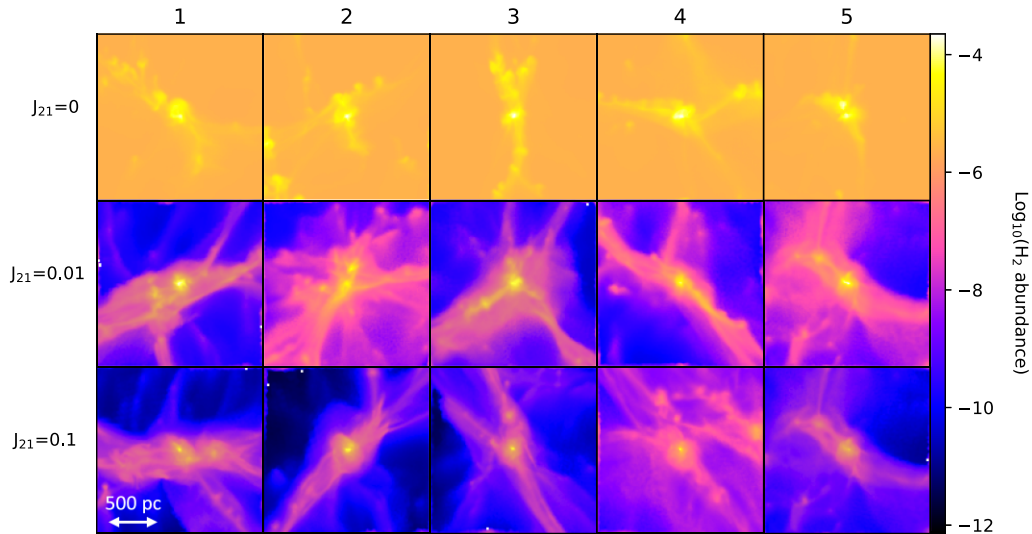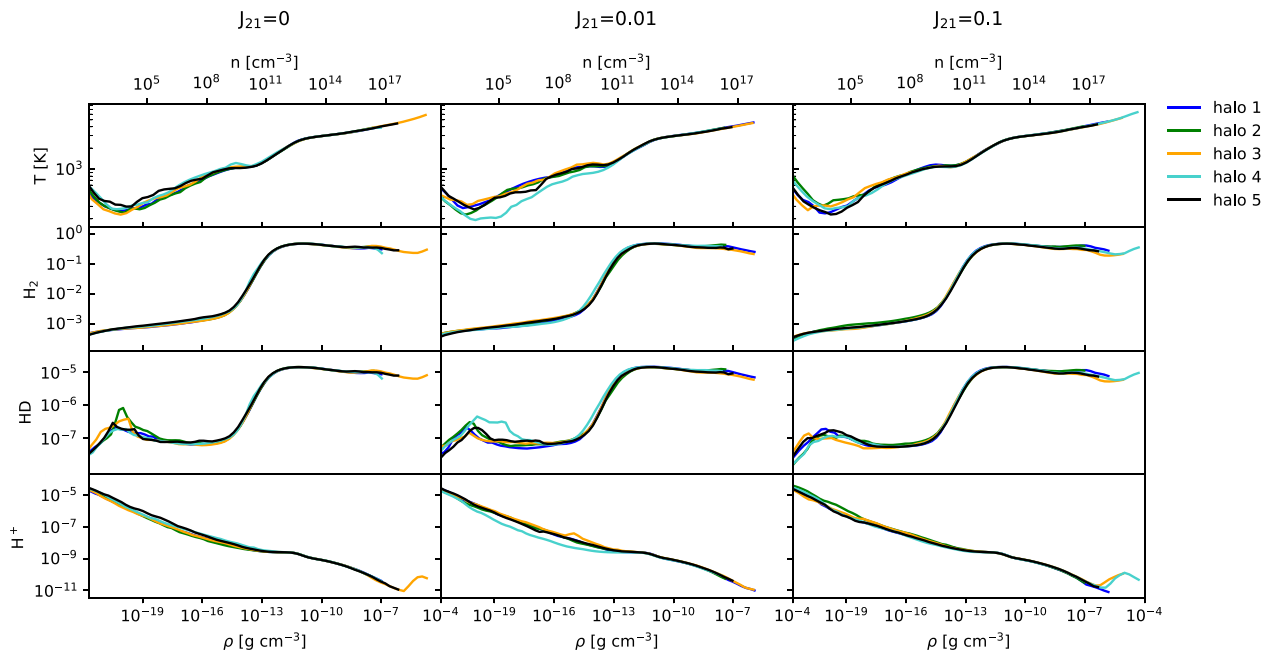
$$\dot{M} = 4\pi R^2 \rho(R) v_{rad}(R) \tag{6}$$

Figure 5. Column-weighted H_2 abundance projections of the 2 kpc region around the 5 cosmological halos for each J_{21} value, taken from AS21, which serve as the initial conditions of the high resolution follow-up simulations presented in this work.

Figure 6. Mass-weighted temperature, H_2, HD, and H^+ abundances versus density at a time shortly after the formation of the first sink particle. (Note that the HD abundance is only tracked self-consistently up to $\rho = 10^{-16}$ g cm^{-3}; above this, we simply fix the HD/H_2 ratio at 2.6×10^{-5}, as explained in Section 2.4).

is our estimate of the mass inflow rate at radius R and $\rho(R)$ and $v_{\rm rad}(R)$ are the mass-weighted density and radial velocity within shells at radius R. For $t_{\rm acc} < 10^4$ yr, there is very little difference between the runs, suggesting that the accretion rate at early times is not influenced by the LW field. For larger $t_{\rm acc}$, we do see a difference between different runs, but this manifests as an increased scatter in $t_{\rm acc}$ at a given R rather than any systematic dependence on the LW field strength.

The right hand side of Fig. 8 shows the gas as it transitions into a fully molecular state within the inner $\sim 10^{-2}$ pc core corresponding to the density regime above 10^{-15} g cm^{-3}. Halos illuminated gy a LW background have higher gas kinetic energies owing to their

larger masses, which promotes a larger molecular core. However, the increasing photodissociation rate with increasing J_{21} acts against this mechanism, reducing the H_2 formation rate and shrinking the molecular core. This results in the $J_{21} = 0.01$ halos having molecular cores that extend to larger radii than the $J_{21} = 0.1$ halos, despite both having larger molecular cores than the $J_{21} = 0$ halos. As we only have access to these three values of J_{21}, the value where the core size is maximized could lie anywhere between $0 < J_{21} < 0.1$.

The importance of the molecular core is shown in Fig. 9, which shows the total mass in sink particles at the end of the simulations as functions of the halo mass, virial temperature, and mass within different regimes of the collapse, just before the maximum density
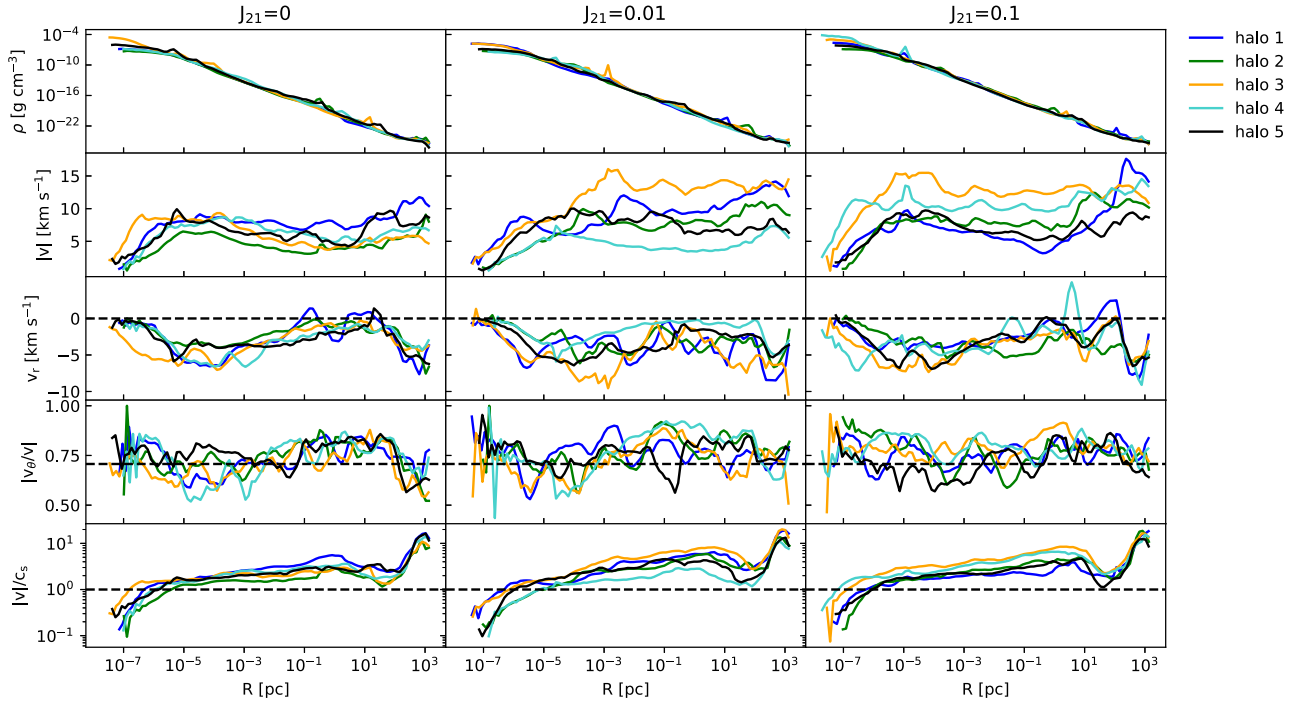
Figure 7. Radial distribution of cumulative gas mass and mass-weighted radial profiles of radial velocity, ratio of rotational to total velocity (note the dotted line represents the value above which rotational component dominates the velocity) and ratio of velocity to sound speed, taken at a time shortly after the formation of the first sink particle.
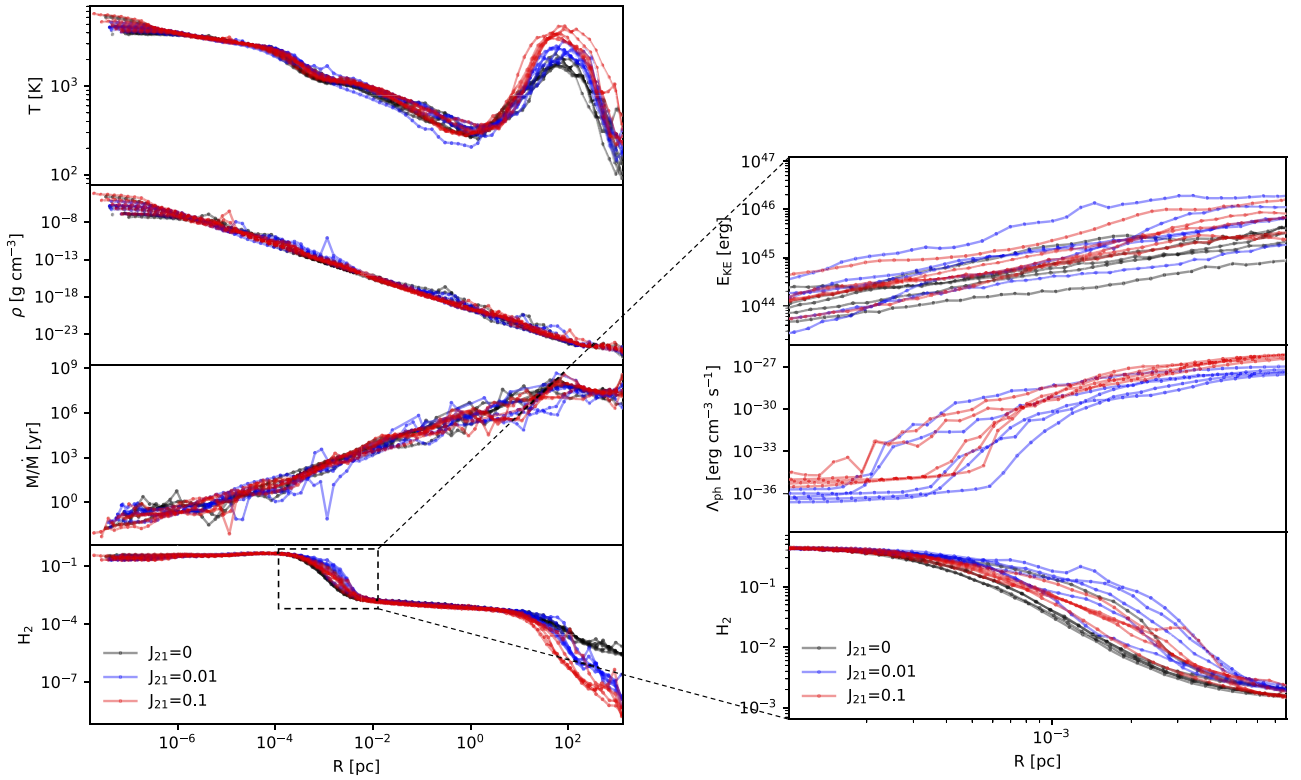

Figure 8. Left: comparison of the mass-weighted temperature, density, and H_2 abundance profiles between the J_{21} values. Right: zoom-in of the transition to fully molecular core, showing the total kinetic energy within radial shells, mass weighted H_2 photodissociation heating rate and H_2 abundance.
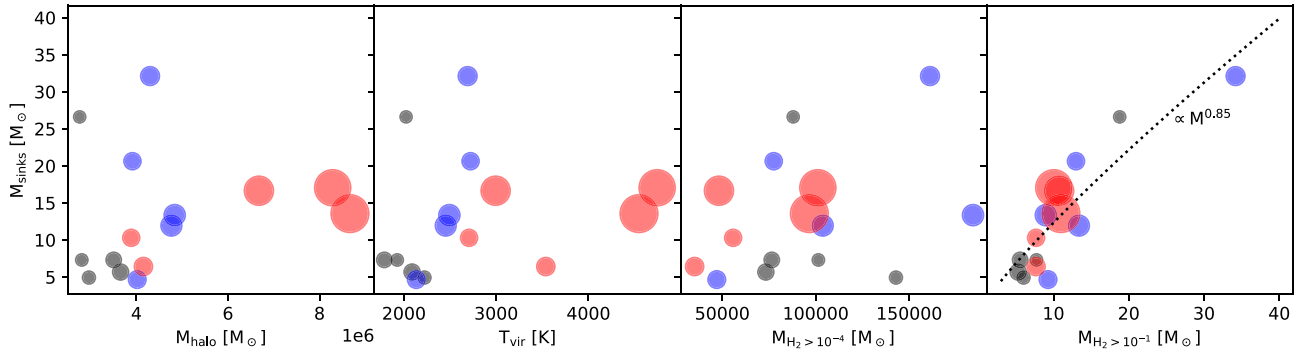
Figure 9. Total mass in sinks at the end of the simulations versus halo mass, virial temperature, mass within the halo with H_2 abundance $>10^{-4}$, and mass within the molecular core with H_2 abundance $>10^{-1}$. The size of the markers is scaled with the halo mass.
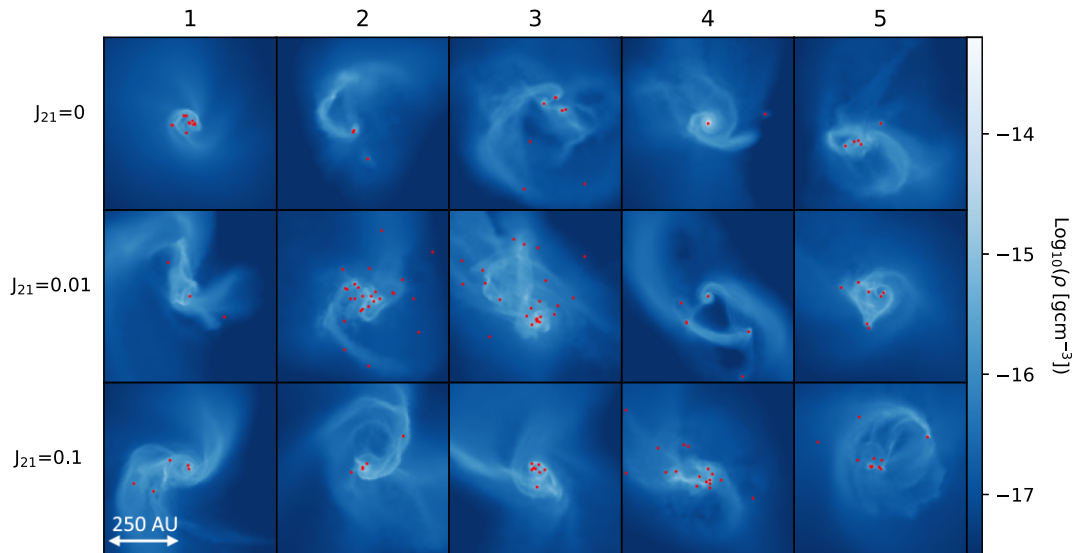
Figure 10. Column-weighted density projections of the inner 650 au of the halos at a time 300 yr after the formation of the first sink particle. Sink particles are represented as red dots.

was reached. The mass in sink particles grows almost linearly with the mass within the inner molecular core with H_2 abundances above 10^{-1} as

$$\log_{10}(M_{sinks}) = (0.85 \pm 0.11)\log_{10}(M_{H_2>10^{-1}}) + (0.14 \pm 0.24). \quad (7)$$

Due to competing effects between halo mass and H_2 photodissociation rate, the mass in sink particles is not correlated with the total halo mass or the subsequent mass that initially falls into its potential well with H_2 abundances $>10^{-4}$. However, we have only followed the accretion for 300 yr, which corresponds to a free-fall time for gas at density $10^{-14}\,\mathrm{g\,cm^{-3}}$. Gas below this density will not have been accreted within the simulation time, while gas above this density resides within the molecular core (see Fig. 6). It is therefore unclear if the relationship between accretion and mass of the molecular core would remain if the simulations ran for a longer time. If the relationship does hold, we speculate that increasing the size of the streaming velocities between gas and DM may have a greater effect on the IMF, since this also increases halo masses without the counteracting effects of H_2 dissociation (Tseliakovich & Hirata 2010; Greif et al. 2011; Hirano et al. 2017; Schauer et al. 2019, AS21).

5 FRAGMENTATION AND THE IMF

The IMF of Pop III stars is determined by the fragmentation behaviour of the disc around the initial central object and the subsequent accretion onto fragments. Density projections of the inner 650 au of the halos are shown in Fig. 10, while Fig. 11 shows the evolution of the total number of sink particles formed, the total mass in sink particles and highest mass sink particle in each halo as a function of time. While the halos from the simulation without a LW background typically yield less fragmentation, the overall fragmentation behaviour is stochastic, as expected. The total mass accreted onto sinks is typically higher in the halos illuminated by a LW field due to their higher halo mass.

Fig. 12 shows the IMF at a time 300 yr after the formation of the first sink particle. The peak of the IMF positioned at $\sim 0.2 - 0.5\,\mathrm{M_\odot}$ shows little dependence on the LW strength, likely because the positive influence of larger halo masses on the molecular core is regulated by the increasing photodissociation rate. We also show the evolution of the cumulative IMFs in time, which converge by the end of the simulations for the $J_{21} = 0.01$ and 0.1 suites. The left side of Fig. 13 compares the combined cumulative IMFs for different J_{21} values. While the high-mass end of the IMFs are nearly identical between the different J_{21} values, the low-mass end of the IMFs show variance due to the random and stochastic nature of ejection events for
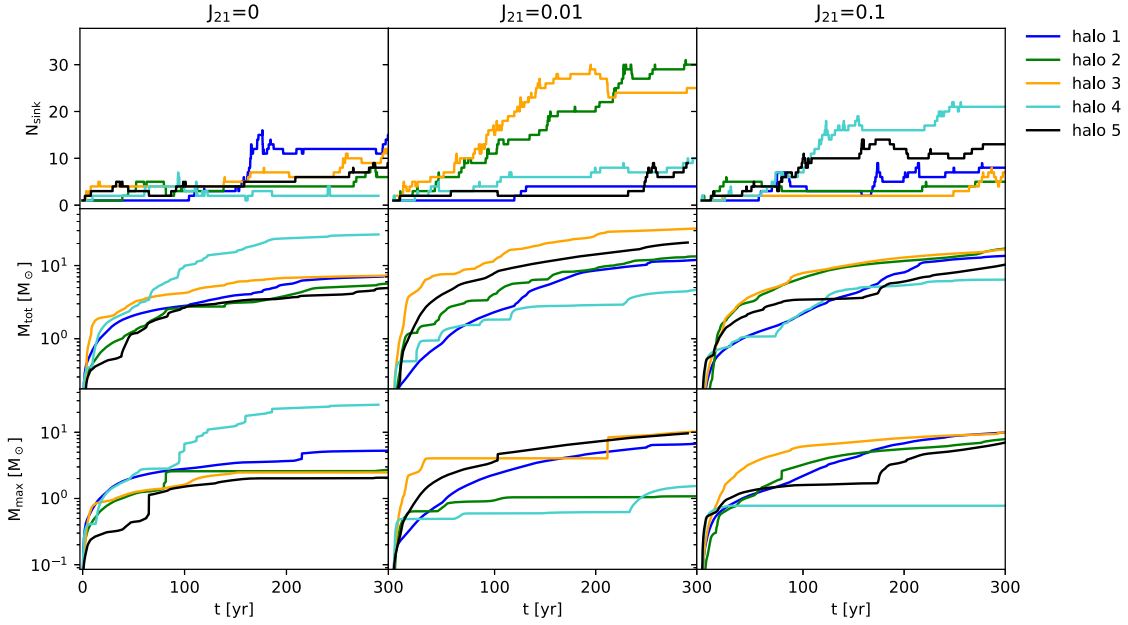
Figure 11. Number of sink particles formed, total mass in sinks, largest mass sink particle, and median mass of sink particles as a function of time.
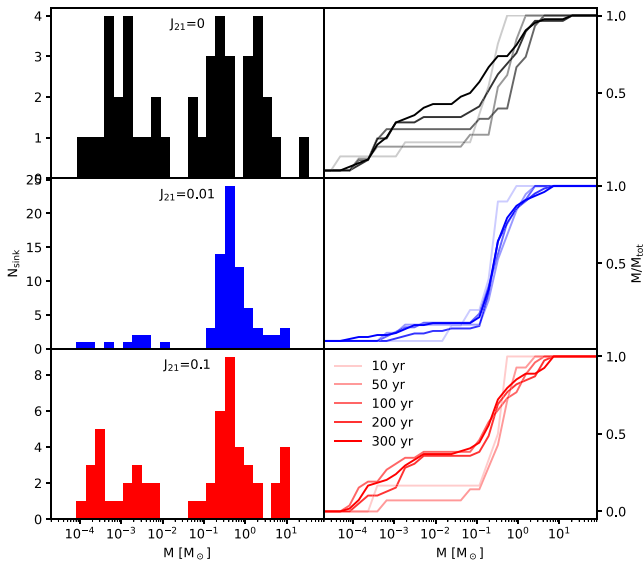

Figure 12. Left: combined IMFs of sink particles for the different the J_{21} values, Right: cumulative IMFs of the combined sink particles for the different the J_{21} values.

We also show the IMF from LP22 as a dotted line, which was produced from idealized halos as opposed the cosmological initial conditions. The cosmological halos produced a bimodal distribution with a significant population of brown dwarfs that the idealized halos are missing. Even when ignoring the brown dwarfs, the cosmological initial conditions have yielded distributions tending to lower mass pre-stellar cores.

To compare the fragmentation behaviour of our simulations with the results of previous studies, we have recreated fig. 10 of Susa (2019) in Fig. 14, which collected data from various studies. They found a power-law growth of the number of fragments with time. As the studies implemented different maximum densities, the time at the end of the simulations was scaled as $\tau/\sqrt{4\pi G \rho_{\rm ad}}$, where $\rho_{\rm ad} = 1.67 \times 10^{-5}$ is the maximum density of Greif et al. (2012) (see Susa 2019 for further details). The fragmentation behaviour in our simulations agrees well with the findings of Susa (2019). Our results appear advanced in time compared to the other studies despite only following 300 yr of fragmentation because of the high-maximum density implemented in this study.

6 CAVEATS

Aside from the obvious uncertainties in the ΛCDM model on which this work and the work of AS21 are based on, there are a number of caveats to note.

The LW fields we have used in this study assume a population of massive Pop III stars already exists. While previous studies do suggest that Pop III stars were massive, more recent work suggests that they may only grow to a few $M_\odot$ (e.g. Stacy & Bromm 2013; Wollenberg et al. 2020; Prole et al. 2022a; Jaura et al. 2022). In this scenario, significantly less LW radiation would be produced, however, radiation from solar mass stars can inhibit H_2 formation through the destruction of H^-. The fields used in this study therefore represent the maximum effect Pop III stars can have on the the Pop III.2 stars that follow. Since the effects of the LW fields appear to be insignificant, it is likely that this result also represents the outcome for weaker fields.
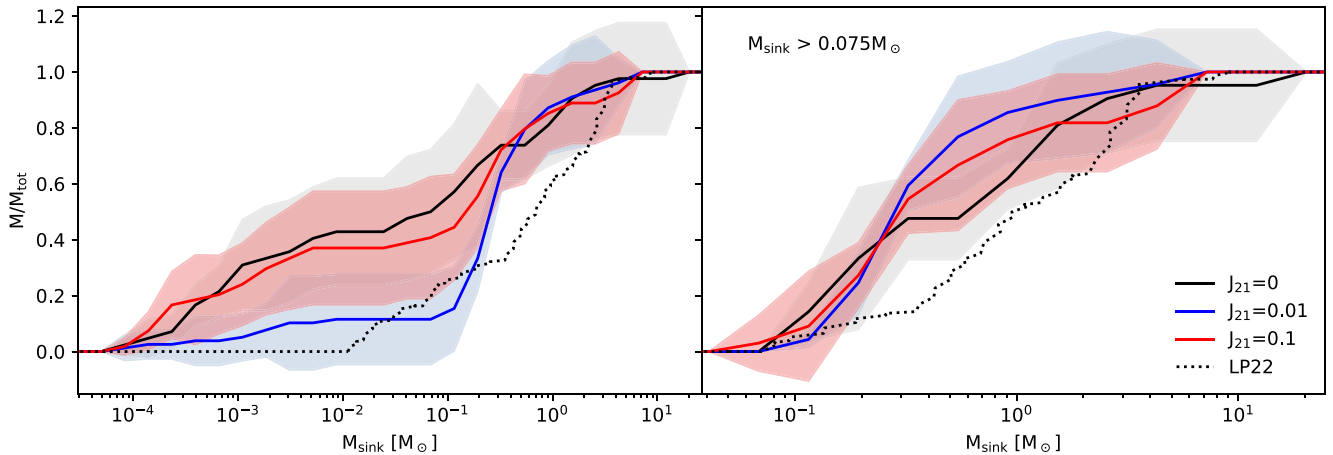
low-mass objects. Assuming these low-mass objects ($<0.075\,M_\odot$) do not go on to accrete significant mass, they will remain as brown dwarfs and never sustain nuclear fusion. The right side of the plot shows the cumulative IMFs if the brown dwarfs are ignored. Here, the IMFs fit well within each other's regions of uncertainty, which are the standard deviations from the cumulative IMFs of the five halos individually. The overlap between the regions of uncertainty indicates that the LW strength does not significantly affect the primordial IMF. As the range of background LW field strengths tested here covers the most likely values from literature, we infer that the IMF for Pop III.2 stars is not significantly different from the initial population of Pop III.1 stars.

Figure 13. Left: comparison of the cumulative IMFs at 300 yr after the formation of the first sink particle. Right: cumulative IMFs ignoring brown dwarfs ($<0.075\,M_\odot$).
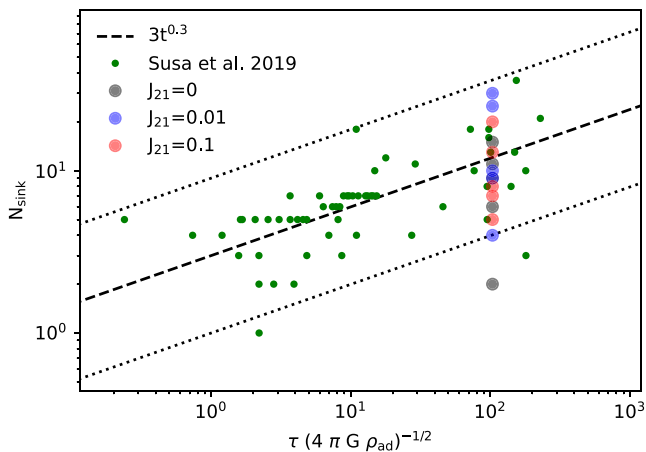

Figure 14. Comparison of the results of our study with the data of various studies collected in fig. 10 of Susa (2019). The number of sink particles formed is plotted versus time-scaled as $\tau/\sqrt{4\pi G \rho_{ad}}$. The thick-dashed line shows the fit $\propto t^{0.3}$ and the dotted lines denote x3 and x1/3 of the thick-dashed line.

The average halo mass from the $J_{21} = 0$ simulations of AS21 are a few times larger than that of Hirano et al. (2015). We assume this is due to the difference in self-shielding treatment, as Hirano et al. (2015) uses the Wolcott-Green et al. (2011) method. For example, an overestimation of self-shielding would result in an underestimation of photodissociation and hence a lower average mass of star forming halos. However, here we have shown that the IMF above the brown dwarf limit is invariant to halo mass.

We have assumed that the pre-stellar core radius grows as equation (5). This process begins immediately after sink particle formation. While this is predicted by stellar theory, it is unclear at what point the pre-stellar core would begin to expand, which may affect the accretion behaviour.

We have neglected the presence of primordial magnetic fields in this study. While the findings of Prole et al. (2022b) suggest that primordial magnetic fields make little difference to the primordial IMF due to their small-scale structure, the field is still active, with other recent studies finding that magnetic fields indeed lead to higher mass Pop III stars (e.g. Saad, Bromm & El Eid 2022; Hirano & Machida 2022; Stacy et al. 2022).

7 CONCLUSIONS

The results of cosmological simulations by AS21 show that increasing the background LW field strength increases the average halo mass required for star formation. These simulations ran up to a maximum density of $10^{-19}\,\mathrm{g\,cm^{-3}}$, hence the knock-on effects on the Pop III IMF were unclear. In this investigation, we have performed follow-up simulations of 5 halos for each of the $J_{21} = 0, 0.01$, and 0.1 LW field strengths, resolving the pre-stellar core density of $10^{-6}\,\mathrm{g\,cm^{-3}}$ before inserting sink particles and following the fragmentation behaviour for hundreds of years further. We have found that the mass accreted onto sinks by the end of the simulations is proportional to the mass within the $\sim 10^{-2}$ pc molecular core, which is not correlated to the initial mass of the halo. As such, the IMF shows little dependence on the LW field strength. We also find no clear relationship between the estimated accretion time of gas lying further out within the halo and the LW field strength, suggesting that the LW field is unlikely to influence the development of the IMF at later times. As the range of background LW field strengths tested here covers the most likely values from literature, we conclude that the IMF for so-called Pop III.2 stars is not significantly different from that of the initial population of Pop III.1 stars, although we cannot rule out greater effects in the small subset of halos that are illuminated by LW fields much stronger than the average value (see e.g Latif et al. 2014). In a future paper, we will explore the effects of increasing the streaming velocities between the gas and DM on the Pop III IMF, as this has been shown to increase halo masses through a different mechanism.

DATA AVAILABILITY

The data underlying this article will be shared on reasonable request to the corresponding author.

REFERENCES

Abel T., Bryan G. L., Norman M. L., 2002, Science (New York, N.Y.), 295, 93
Abel T., Wise J. H., Bryan G. L., 2007, ApJ, 659, L87
Agarwal B., Khochfar S., 2015, MNRAS, 446, 160
Agarwal B., Khochfar S., Johnson J. L., Neistein E., Dalla Vecchia C., Livio M., 2012, MNRAS, 425, 2854
Agarwal B., Dalla Vecchia C., Johnson J. L., Khochfar S., Paardekooper J.-P., 2014, MNRAS, 443, 648
Agarwal B., Smith B., Glover S., Natarajan P., Khochfar S., 2016, MNRAS, 459, 4209
Ahn K., Shapiro P. R., Iliev I. T., Mellema G., Pen U.-L., 2009, ApJ, 695, L1430
Alvarez M. A., Bromm V., Shapiro P. R., 2006, ApJ, 639, 621
Beers T. C., Christlieb N., 2005, ARA&A, 43, 531
Bromm V., Loeb A., 2003, ApJ, 596, L34
Bromm V., Coppi P. S., Larson R. B., 2002, ApJ, 564, L23
Chuzhoy L., Kuhlen M., Shapiro P. R., 2007, ApJ, 665, L85
Clark P. C., Glover S. C. O., Smith R. J., Greif T. H., Klessen R. S., Bromm V., 2011, Science, 331, 1040
Clark P. C., Glover S. C. O., Klessen R. S., 2012, MNRAS, 420, 745
Collaboration P., et al., 2020, A&A, 641, 6
Couchman H. M. P., Rees M. J., 1986, MNRAS, 221, 53
Dijkstra M., Haiman Z., Mesinger A., Wyithe J. S. B., 2008, MNRAS, 391, 1961
Draine B. T., Bertoldi F., 1996, ApJ, 468, L269
Eisenstein D. J., Hu W., 1998, ApJ, 496, L605
Field G. B., Somerville W. B., Dressler K., 1966, ARA&A, 4, 207
Frebel A., Norris J. E., 2015, ARA&A, 53, 631
Glover S. C. O., 2015, MNRAS, 451, 2082
Glover S. C. O., Abel T., 2008, MNRAS, 388, 1627
Glover S. C., Savin D. W., Jappsen A.-K., 2006, ApJ, 640, L553
Greif T. H., White S. D. M., Klessen R. S., Springel V., 2011, ApJ, 736, L147
Greif T. H., Bromm V., Clark P. C., Glover S. C. O., Smith R. J., Klessen R. S., Yoshida N., Springel V., 2012, MNRAS, 424, 399
Hahn O., Abel T., 2011, MNRAS, 415, 2101
Haiman Z., Thoul A. A., Loeb A., 1996a, ApJ, 464, L523
Haiman Z., Thoul A. A., Loeb A., 1996b, ApJ, 464, L523
Haiman Z., Rees M. J., Loeb A., 1997, ApJ, 476, L458
Haiman Z., Abel T., Rees M. J., 2000, ApJ, 534, L11
Hartwig T., Glover S. C. O., Klessen R. S., Latif M. A., Volonteri M., 2015a, MNRAS, 452, 1233
Hartwig T., Clark P. C., Glover S. C. O., Klessen R. S., Sasaki M., 2015b, ApJ, 799, L114
Heitmann K., et al., 2008, Computational Science and Discovery, 1, 015003
Hirano S., Machida M. N., 2022, ApJ, 935, L16
Hirano S., Hosokawa T., Yoshida N., Umeda H., Omukai K., Chiaki G., Yorke H. W., 2014, ApJ, 781, L60
Hirano S., Hosokawa T., Yoshida N., Omukai K., Yorke H. W., 2015, MNRAS, 448, 568
Hirano S., Hosokawa T., Yoshida N., Kuiper R., 2017, Science, 357, 1375
Hosokawa T., Omukai K., 2009, ApJ, 691, L823
Hosokawa T., Omukai K., Yorke H. W., 2012, ApJ, 756, L93
Jaura O., Glover S. C. O., Wollenberg K. M. J., Klessen R. S., Geen S., Haemmerlé L., 2022, MNRAS, 512, 116
Johnson J. L., Khochfar S., 2011, MNRAS, 413, 1184
Kitayama T., Yoshida N., Susa H., Umemura M., 2004, ApJ, 613, L631
Kulkarni M., Visbal E., Bryan G. L., 2021, ApJ, 917, L40
Latif M. A., Schleicher D. R. G., Schmidt W., Niemeyer J. C., 2013, MNRAS, 436, 2989
Latif M. A., Schleicher D. R. G., Bovino S., Grassi T., Spaans M., 2014, ApJ, 792, L78
Ma C.-P., Bertschinger E., 1995, ApJ, 455, L7
Machacek M. E., Bryan G. L., Abel T., 2001, ApJ, 548, L509
Machida M. N., Doi K., 2013, MNRAS, 435, 3283
Machida M. N., Nakamura T., 2015, MNRAS, 448, 1405
Matsuoka Y., et al., 2019, ApJ, 872, L2
Monaghan J. J., 1992, ARA&A, 30, 543
Mortlock D. J., et al., 2011, Nature, 474, 616
O'Shea B. W., Norman M. L., 2008, ApJ, 673, L14
Oh S. P., Haiman Z., 2002, ApJ, 569, L558
Omukai K., 2001, ApJ, 546, L635
Omukai K., Palla F., 2003, ApJ, 589, L677
Prole L. R., Clark P. C., Klessen R. S., Glover S. C. O., 2022a, MNRAS, 510, 4019
Prole L. R., Clark P. C., Klessen R. S., Glover S. C. O., Pakmor R., 2022b, MNRAS, 516, 2223
Regan J. A., Johansson P. H., Wise J. H., 2014, ApJ, 795, L137
Saad C. R., Bromm V., El Eid M., 2022, MNRAS, 516, 3130
Schaerer D., 2002, A&A, 382, 28
Schauer A. T. P., Glover S. C. O., Klessen R. S., Ceverino D., 2019, MNRAS, 484, 3510
Schauer A. T. P., Glover S. C. O., Klessen R. S., Clark P., 2021, MNRAS, 507, 1775
Shang C., Bryan G. L., Haiman Z., 2010, MNRAS, 402, 1249
Skinner D., Wise J. H., 2020, MNRAS, 492, 4386
Smith R. J., Glover S. C. O., Clark P. C., Greif T., Klessen R. S., 2011, MNRAS, 414, 3633
Spaans M., Silk J., 2006, ApJ, 652, L902
Springel V., 2010, MNRAS, 401, 791
Stacy A., Bromm V., 2013, MNRAS, 433, 1094
Stacy A., Pawlik A. H., Bromm V., Loeb A., 2014, MNRAS, 441, 822
Stacy A., McKee C. F., Lee A. T., Klein R. I., Li P. S., 2022, MNRAS, 511, 5042
Stahler S., Palla F., Salpeter E., 1986, ApJ, 302, L90
Starkenburg E., et al., 2017, MNRAS, 471, 2587
Stecher T. P., Williams D. A., 1967, ApJ, 149, L29
Sugimura K., Omukai K., Inoue A. K., 2014, MNRAS, 445, 544
Susa H., 2019, ApJ, 877, L99
Tanaka S. J., Chiaki G., Tominaga N., Susa H., 2017, ApJ, 844, L137
Tegmark M., Silk J., Rees M. J., Blanchard A., Abel T., Palla F., 1997, ApJ, 474, L1
Trenti M., Stiavelli M., 2009, ApJ, 694, L879
Tress R. G., Smith R. J., Sormani M. C., Glover S. C. O., Klessen R. S., Mac Low M.-M., Clark P. C., 2020, MNRAS, 492, 2973

Tseliakhovich D., Hirata C., 2010, Physical Rev. D, 82, 083520

Turk M. J., Clark P., Glover S. C. O., Greif T. H., Abel T., Klessen R., Bromm V., 2011, ApJ, 726, L55

Visbal E., Haiman Z., Terrazas B., Bryan G. L., Barkana R., 2014, MNRAS, 445, 107

Whalen D., Abel T., Norman M. L., 2004, ApJ, 610, L14

Wise J. H., Abel T., Turk M. J., Norman M. L., Smith B. D., 2012, MNRAS, 427, 311

Wolcott-Green J., Haiman Z., Bryan G. L., 2011, MNRAS, 418, 838

Wollenberg K. M. J., Glover S. C. O., Clark P. C., Klessen R. S., 2020, MNRAS, 494, 1871

Yoshida N., Abel T., Hernquist L., Sugiyama N., 2003, ApJ, 592, L645

Yoshida N., Omukai K., Hernquist L., Abel T., 2006, ApJ, 652, L6

Yoshida N., Oh S. P., Kitayama T., Hernquist L., 2007a, ApJ, 663, L687

Yoshida N., Omukai K., Hernquist L., 2007b, ApJ, 667, L117

This paper has been typeset from a TEX/LATEX file prepared by the author.